

## Measurements of spectral lines observed with Hinode/EIS as implications for coronal heating \*

Ying Li and Ming-De Ding

Department of Astronomy, Nanjing University, Nanjing 210093, China; [dmd@nju.edu.cn](mailto:dmd@nju.edu.cn)

Received 2008 December 11; accepted 2009 March 2

**Abstract** We have measured the line widths and nonthermal velocities in 12 solar regions using high resolution EUV data taken by Hinode/EIS. We find that there exists a positive correlation between the intensity and nonthermal velocity for the Fe XII emission line as well as some other lines. The correlation coefficients decrease from the disk center to the limb. However, the nonthermal velocities of a particular spectral line do not vary much in different regions, so they are considered isotropic. In particular, we find that for a coronal loop structure, the largest widths and nonthermal velocities occur at the footpoints, where outflows appear. Based on these observational results, we discuss several physical processes responsible for coronal heating.

**Key words:** line: profiles — Sun: corona — Sun: UV radiation

### 1 INTRODUCTION

The coronal heating problem, the puzzle of what maintains the solar corona two orders of magnitude hotter than the photosphere, is one of the outstanding questions in solar physics. So far, various physical processes have been proposed as possible heating mechanisms, including acoustic waves (Biermann 1946; Schwarzschild 1948; Suzuki 2002), Alfvén waves (Zirker 1993), magnetoacoustic waves (Cheng et al. 1979), nanoflares (Parker 1988; Zirker & Cleveland 1993), MHD turbulence (Chae et al. 1998; Inverarity et al. 1995), and electric currents (Zirker 1993). Aschwanden (2004) categorized theoretical models of coronal heating into five groups, according to the main physical processes involved. These are: (1) DC (Direct Current) stressing and reconnection models (e.g., stress-induced reconnection, stress-induced turbulence), (2) AC (Alternating Current) wave heating models (e.g., Alfvénic resonance, MHD turbulence etc.), (3) acoustic heating, (4) chromospheric reconnection, and (5) velocity filtration. Furthermore, Tsiklauri (2005) investigated the possibility of heating the loops and other closed magnetic structures in active regions by the flow of solar wind (plus other flows that may be present) across the magnetic field lines, in a similar manner to a conventional MHD generator. Due to the limitations of observational instruments and theoretical development, however, none of these mechanisms is confirmed unambiguously at present.

Previous EUV measurements (Boland et al. 1975; Doschek et al. 1976; Dere & Mason 1993) have revealed that most solar EUV lines are broader than those expected from thermal broadening, which is usually regarded as a manifestation of unresolved mass motions (nonthermal motions) of the plasma. The nonthermal motions could be referred to as multiple flows, turbulence or waves, each of which may play a role in energy transport and heating in the corona. Chae et al. (1998) have examined the nonthermal velocities inferred from a number of EUV and far-ultraviolet (FUV) lines observed by SUMER,

---

\* Supported by the National Natural Science Foundation of China.

which implicates possible coronal heating mechanisms. This motivates us to seek more observational evidence to interpret the coronal heating problem based upon the measurements of spectral lines in the solar upper atmosphere.

The Extreme-ultraviolet Imaging Spectrometer (EIS) instrument on board the Hinode satellite, launched on 2006 September 23, provides us with EUV line data with unprecedented high spectral and spatial resolution for studying nonthermal motions. By measuring the excess line widths, we can investigate coronal dynamics. In this paper, we study the EUV lines in 12 regions and draw results that may shed light on the coronal heating mechanisms.

## 2 OBSERVATIONS AND DATA REDUCTION

Hinode's EIS (Culhane et al. 2007; Kosugi et al. 2007) is a high performance stigmatic instrument for observing the solar atmosphere in the 170–210 Å and 250–290 Å wavelength regions with a spectral resolution of  $0.0223 \text{ \AA pixel}^{-1}$ . The peak efficiency is achieved at 195 Å for the shorter wavelengths and at 270 Å for the longer wavelengths. These two bands include strong emission lines that are formed at  $10^{4.7}$ – $10^{7.3}$  K. The EIS can image the Sun using 1'' and 2'' slits and 40'' and 266'' slots, and can operate in several modes. For the data described in this study, the 1'' slit was used and was rastered west to east across a region in 1'' steps.

The observations discussed here cover 12 solar regions at different positions (see Fig. 1). Most of them are active regions (ARs). Nevertheless, a quiet Sun region (QS) is also taken into account. These regions are distributed from the disk center to the limb. Table 1 lists their information, including the observation time, field of view, location, exposure time, and line window.

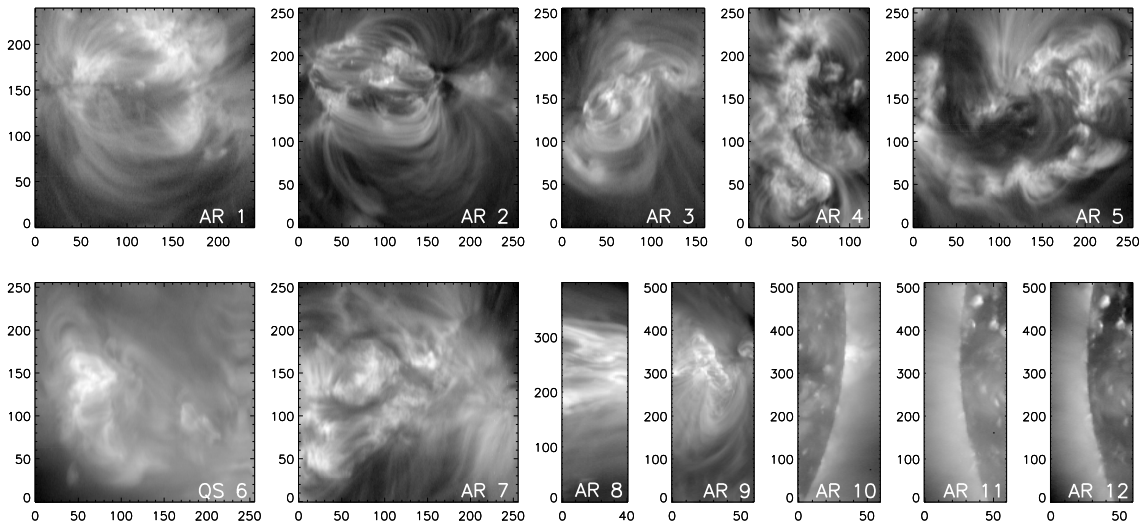


**Fig. 1** Intensity maps of all the 12 regions at the Fe XII  $\lambda 195.12$  line.

The EIS can observe in at most 25 spectral windows in each scan, and usually uses more than ten windows. Therefore, we face a problem of selecting lines. Those lines that are strong enough to have good signal-to-noise ratios are preferable for study. The shape of the effective area (EA) curves is an important factor when choosing emission lines. Another factor that we have to consider is the degree of blending. Many lines are blended with others, such as Ca XVII  $\lambda 192.82$  with Fe XI  $\lambda 192.83$ , and He II  $\lambda 256.32$  with Si X  $\lambda 256.37$ . Besides the weak and blended lines, we discard the saturated ones. In the active regions, a few of the strongest lines were saturated in a long exposure. For these reasons, we only

**Table 1** Parameters of the Observed Solar Regions Selected for Study

Number	NOAA	Observation Time (yyyymmdd hhmmss)	FOV (arcsec <sup>2</sup> )	Location	Exposure (s)	Line Window
AR 1	10938	20070119 043749	240×240	(334'', 97'')	5.0	17
AR 2	10926	20061202 140632	256×256	(298'', -163'')	10.0	15
AR 3	10955	20070513 124706	256×256*	(540'', -110'')	10.0	17
AR 4	10953	20070430 154423	120×256	(-147'', -97'')	20.0	17
AR 5	10940	20070202 104212	256×256	(333'', 30'')	15.0	20
QS 6		20061226 112050	256×256	(-636'', -105'')	30.0	9
AR 7	10980	20080106 105243	256×256	(-252'', -44'')	15.0	20
AR 8	10980	20080104 101728	41×400	(-457'', -51'')	30.0	20
AR 9	10978	20071208 064040	60×512	(-658'', -152'')	50.0	25
AR 10		20071015 114535	60×512	(-940'', -100'')	50.0	25
AR 11		20071021 234434	60×512	(-945'', 0'')	50.0	25
AR 12		20071022 003634	60×512	(-945'', 0'')	50.0	25

\*The actual FOV is  $256 \times 256$  arcsec<sup>2</sup>. Here we only use a partial region of  $160 \times 256$  arcsec<sup>2</sup>, owing to a lack of data in the remainder of the region.

use the relatively strong, unblended and non-saturated emission lines. Therefore, the Fe XII  $\lambda 195.12$  line (near the peak efficiency wavelength) is our favored line. There is a need to emphasize that the observed width of the 195.12 Å line is slightly larger than the widths of the other Fe XII lines. A possible reason is blending with a relatively weak Fe XII line at 195.18 Å, but this does not affect our results substantially. Table 2 shows the lines selected for measurements of nonthermal motions. These lines are taken from the same slit image so that they have exactly the same observing time and pointing direction. Each line in the solar atmosphere is formed over a characteristic narrow temperature range. Quantity  $T_{\max}$  in the table denotes the temperature of maximum abundance.

**Table 2** Iron Lines Used for Analysis

Ions	Wavelength (Å)	$\log T_{\max}$ (K)
Fe XI	180.40	6.1
Fe XII	195.12	6.1
Fe XIII	202.04	6.2
Fe XIV	264.78	6.3
Fe XV	284.16	6.3
Fe XVI	262.98	6.4
Fe XXIV	191.13	7.2

We reduce the data using the current version of the EIS data preparation software. This includes the correction of detector bias and dark current, as well as hot pixels and cosmic ray hits, resulting in absolute intensities in  $\text{erg cm}^{-2} \text{s}^{-1} \text{sr}^{-1} \text{Å}^{-1}$ . We then measure the line width at every spatial grid of size  $1'' \times 1''$  in a given field of view by applying Gaussian fitting to the observed line profiles. For an optically thin line, if the ion and electron temperatures are equal and the instrumental width is known and removed from the line width, then the full width at half maximum of a spectral line is related to the nonthermal velocity,  $\xi$ , by (e.g., Mariska 1992)

$$W = 1.665 \frac{\lambda}{c} \sqrt{\frac{2kT}{M} + \xi^2}, \quad (1)$$

where  $\lambda$  is the wavelength (in units of Å),  $c$  is the speed of light,  $k$  is the Boltzmann constant,  $T$  is the electron temperature, and  $M$  is the ion mass. We adopted an in-orbit instrumental width of 2.5 pixels, or 0.056 Å. Note that we assume that the profiles are mostly Gaussian. In addition, we ignore the line profiles whose total FWHMs are less than the instrumental width in the following analysis.

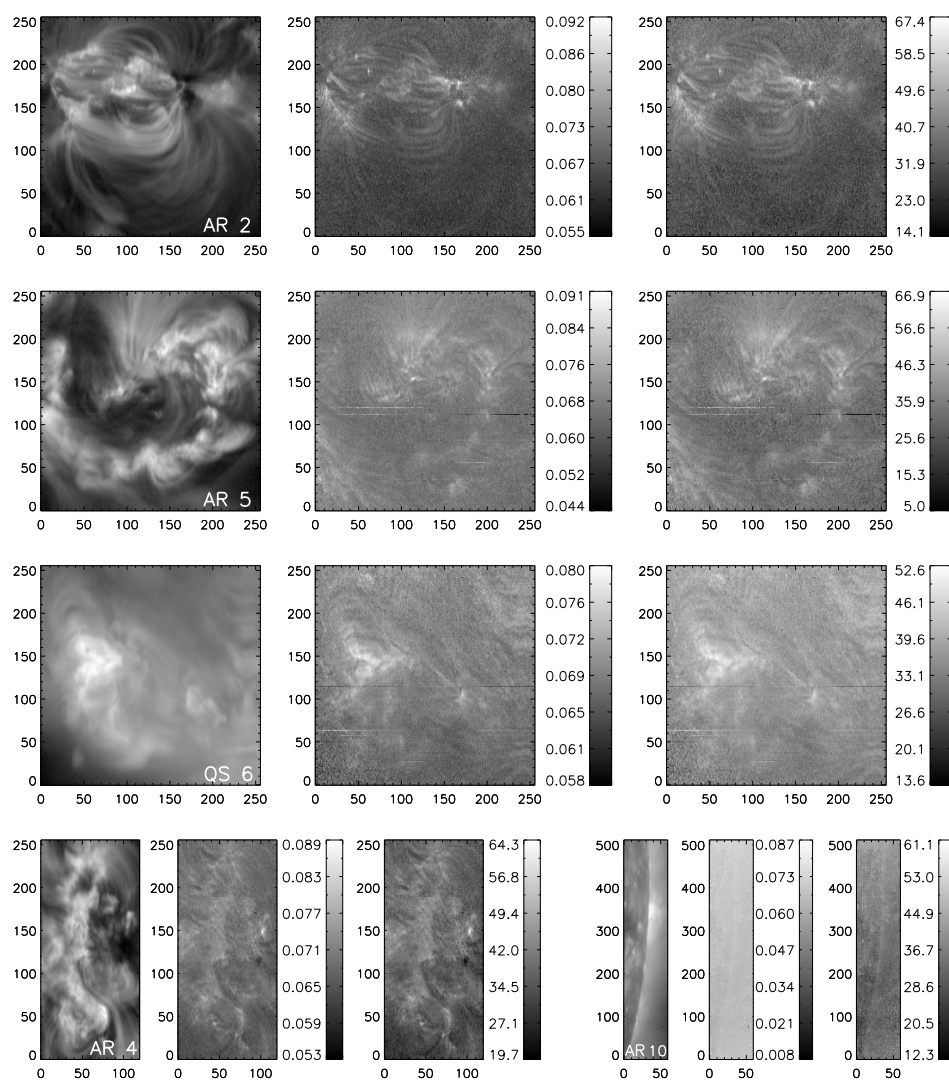


**Fig. 2** Images of the Fe XII  $\lambda 195.12$  line for 5 regions. Each panel stands for a region. Left: Line intensity. Middle: Line width. The color bars are in units of  $\text{\AA}$ . Right: Nonthermal velocity. The color bars are in units of  $\text{km s}^{-1}$ .

### 3 RESULTS

#### 3.1 Spatial Distribution

We first measure the Fe XII  $\lambda 195.12$  emission line because of its high signal-to-noise ratio. Five regions are selected as shown in Figure 2. At first glance, we can see that the loop, flare, or limb structures appear in the width map and the nonthermal velocity map, similar to that in the line intensity image. However, careful inspection shows that the largest widths do not occur at the peak intensities but are adjacent to them, as previously pointed out by Doschek et al. (2007). Regardless of this, there is a positive

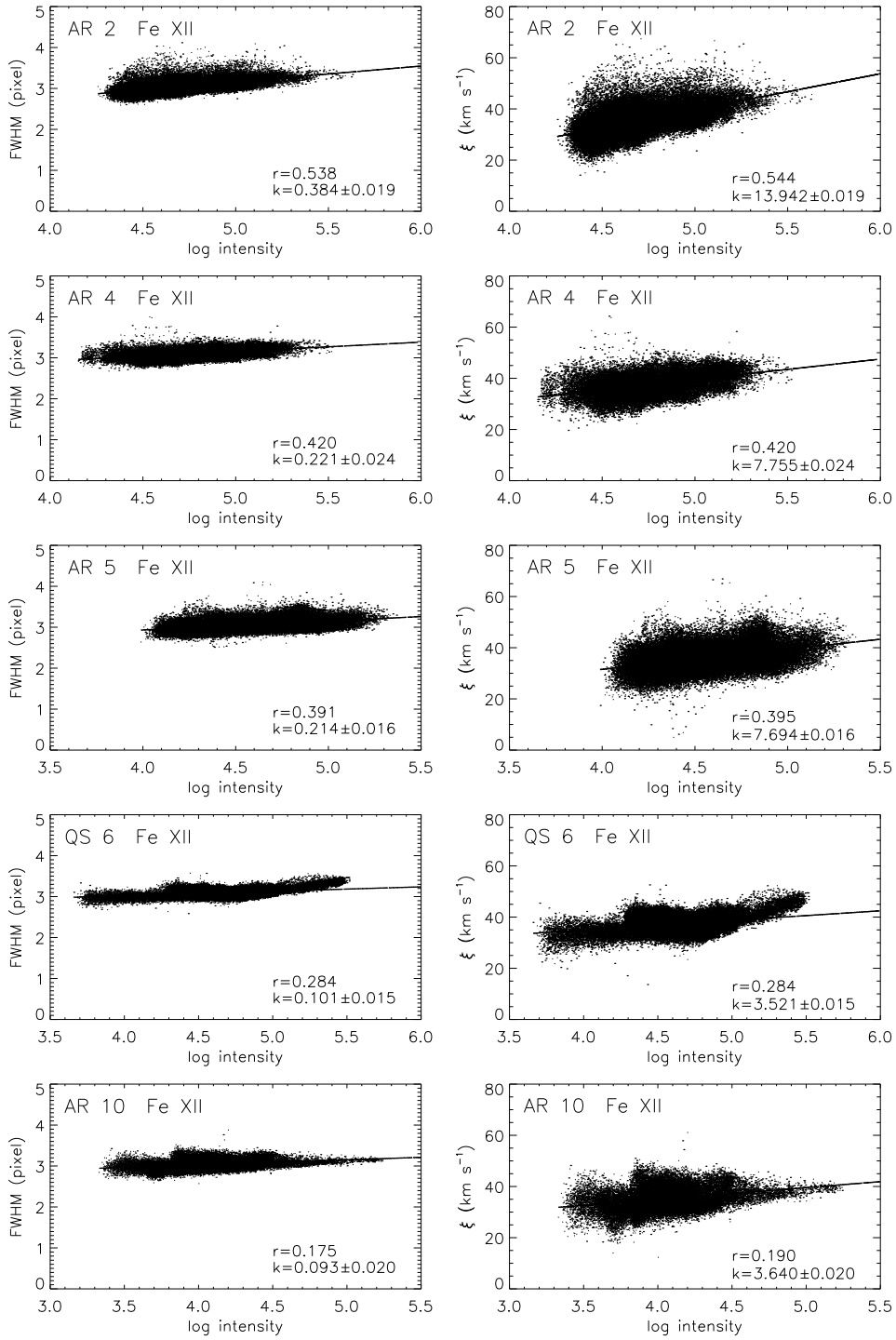


**Fig. 3** Scatter plots of line width and nonthermal velocity versus logarithmic intensity for Fe XII  $\lambda 195.12$  line. The correlation coefficient,  $r$ , and the slope of the fitting curve,  $k$ , are shown for each case. The intensity is in units of  $\text{erg cm}^{-2} \text{s}^{-1} \text{sr}^{-1} \text{\AA}^{-1}$ .

correlation between the nonthermal motion and the line intensity in general. We show the scatter plots in Figure 3 and calculate the correlation coefficients between them. Note that the coefficient can reach 0.544 for AR 2. An even higher value of 0.678 is obtained for loops (see Sect. 3.3). This indicates a fairly strong correlation between the two parameters.

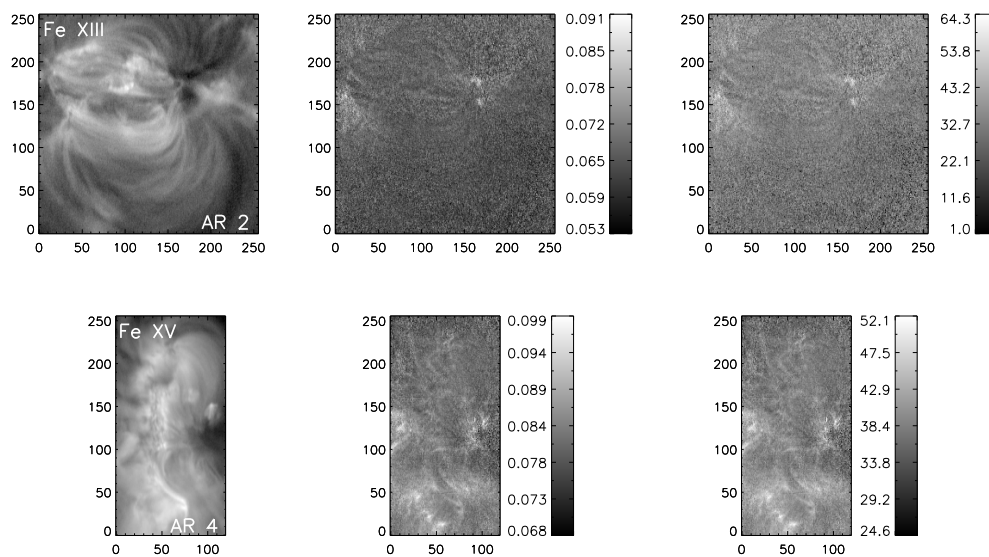


**Fig. 4** Images of the Fe XIII  $\lambda 202.04$  and Fe XV  $\lambda 284.16$  lines. From left to right: Line intensity, line width and nonthermal velocity. The color bars are in units of  $\text{\AA}$  and  $\text{km s}^{-1}$ , respectively.

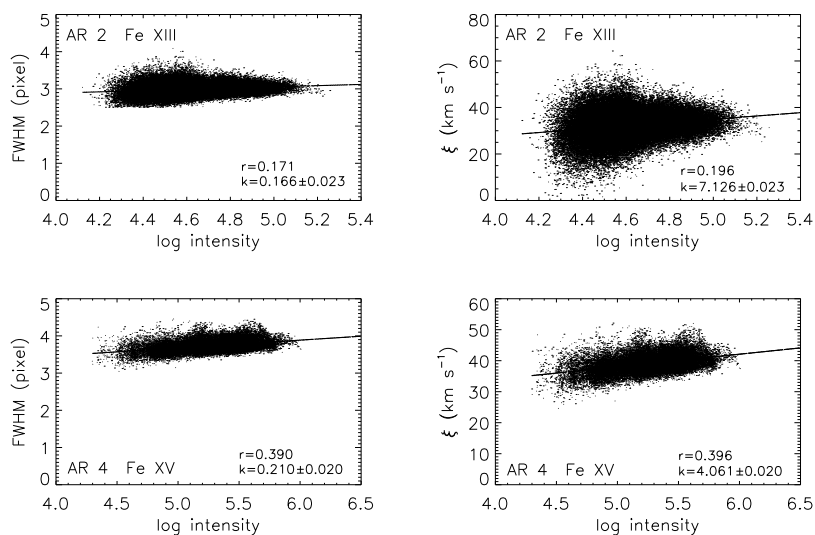


**Fig. 5** Scatter plots of line width and nonthermal velocity versus logarithmic intensity for Fe XIII  $\lambda 202.04$  and Fe XV  $\lambda 284.16$  lines. The correlation coefficient,  $r$ , and the slope of the fitting curve,  $k$ , are shown for each case. The intensity is in units of  $\text{erg cm}^{-2} \text{s}^{-1} \text{sr}^{-1} \text{\AA}^{-1}$ .

Similar correlations between the line width (or nonthermal velocity) and the line intensity exist in other emission lines like the Fe XIII  $\lambda 202.04$  and Fe XV  $\lambda 284.16$  lines as illustrated in Figures 4 and 5. However, the correlations are not so obvious as compared with the case of the Fe XII  $\lambda 195.12$  line. In principle, there are two reasons for this. One is the sensitivity of EIS at different wavelengths, and the other is the line intensity itself. When the line intensity does not show enough contrast with the background, the results suffer big uncertainties. An interesting finding is that the correlations vary in different regions, showing a dependence on structures in monochromatic images. For QS 6, as shown in Figure 3, the scatter plots have two components at lower and higher intensities. The higher intensity portion corresponds to a nanoflare and shows a stronger relationship between the nonthermal velocity and the line intensity. We will discuss this result further below.

### 3.2 Center-to-Limb Variation

#### 3.2.1 Correlation coefficient

The correlation coefficients calculated for the 12 regions using the Fe XII  $\lambda 195.12$  line are given in Table 3, together with the spatially averaged nonthermal velocities. Here, we only list the results for the Fe XII  $\lambda 195.12$  line for the sake of detector sensitivity, line intensity, and CCD bug, etc.. We roughly classify the 12 images into three groups: loop-like, flare-like, and limb structures. As can be seen in the table, the correlation coefficients between the line intensity and nonthermal velocity vary over a wide range, from more than 0.65 to nearly zero. Now we check the center-to-limb dependence. Figure 6 shows the variation of the coefficients as a function of the projected radius.

**Table 3** Correlation Coefficients and Spatially Averaged Nonthermal Velocities for 12 Regions Derived from the Fe XII  $\lambda 195.12$  Line

Regions	Correlation coefficients		$\bar{\xi}$ (km s <sup>-1</sup> )	Note
	log $I$ – FWHM	log $I$ – $\xi$		
AR 1	0.646	0.655	37.75	loop-like
AR 2	0.538	0.544	35.24	loop-like
AR 3	0.427	0.440	33.69	loop-like
AR 4	0.420	0.420	37.72	flare-like
AR 5	0.391	0.396	35.95	flare-like
QS 6	0.284	0.284	37.45	flare-like
AR 7	0.245	0.271	35.12	flare-like
AR 8	0.185	0.222	34.72	flare-like
AR 9	0.193	0.206	35.59	flare-like
AR 10	0.175	0.190	36.03	limb
AR 11	0.062	0.080	36.34	limb
AR 12	-0.002	0.016	36.23	limb

Figure 6 clearly shows that the coefficients decrease from the center to the limb. Also, loop structures seem to show a stronger correlation between the line intensity and nonthermal motion than other structures. Regardless of the different correlation coefficients, different structures obey similar center-to-limb variations.

#### 3.2.2 Nonthermal velocity

Similarly, we also examine how the nonthermal velocity depends on position on the solar disk. Figure 7 displays the result, together with the line intensity distribution. The left panel shows the nonthermal velocities of the Fe XII line (see also Table 3). We find that the nonthermal velocity hardly varies from the disk center to the limb. It fluctuates trivially around 36 km s<sup>-1</sup>. In order to confirm this result, we plot the nonthermal velocity for the Fe XIII  $\lambda 202.04$  line in the right panel of Figure 7. The two lines

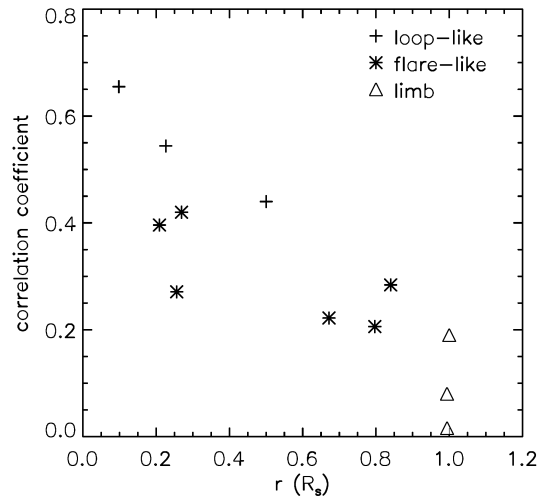


**Fig. 6** Variation of the correlation coefficients between the line intensity and nonthermal velocity as a function of projected radius normalized to the solar radius for the Fe XII  $\lambda 195.12$  line. Crosses, asterisks, and triangles represent loop-like, flare-like, and limb structures, respectively.

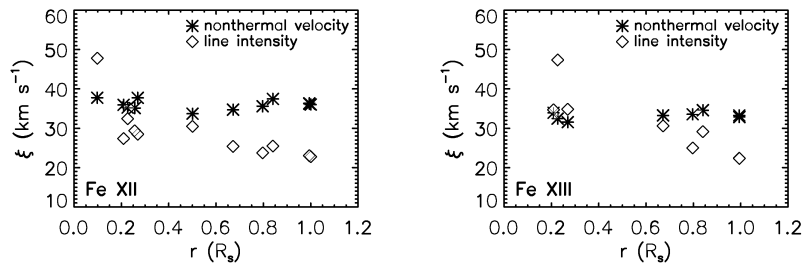


**Fig. 7** Distribution of nonthermal velocity with respect to projected radius. The line intensity, in arbitrary units, is plotted as well. The left and right panels show the results for the Fe XII  $\lambda 195.12$  and Fe XIII  $\lambda 202.04$  lines, respectively.

show the same result. We can then draw a conclusion that the nonthermal motions are basically isotropic, confirming the previous results by Mariska et al. (1978), Chae et al. (1998), and Gan & Li (2002).

Actually, the spatially averaged line intensities show a decrease from the disk center to the limb after unifying the exposure time (see Fig. 7). This implies that the signal-to-noise ratio is relatively low in limb cases. Considering the isotropy of nonthermal velocities, we can naturally obtain the center-to-limb variation of the correlation coefficients between the line intensity and nonthermal velocity.

### 3.3 Loop Structure

As described in Section 3.2.1, obvious loop structures show stronger correlations between the line intensity and nonthermal velocity. ARs 1–3 contain three large loops. Figure 8 illustrates the line intensity, line width, nonthermal velocity, and Doppler shift for the three regions. The arrows indicate the foot-points of the loops, which can be most clearly seen in the Fe VIII  $\lambda 185.21$  line intensity image. The

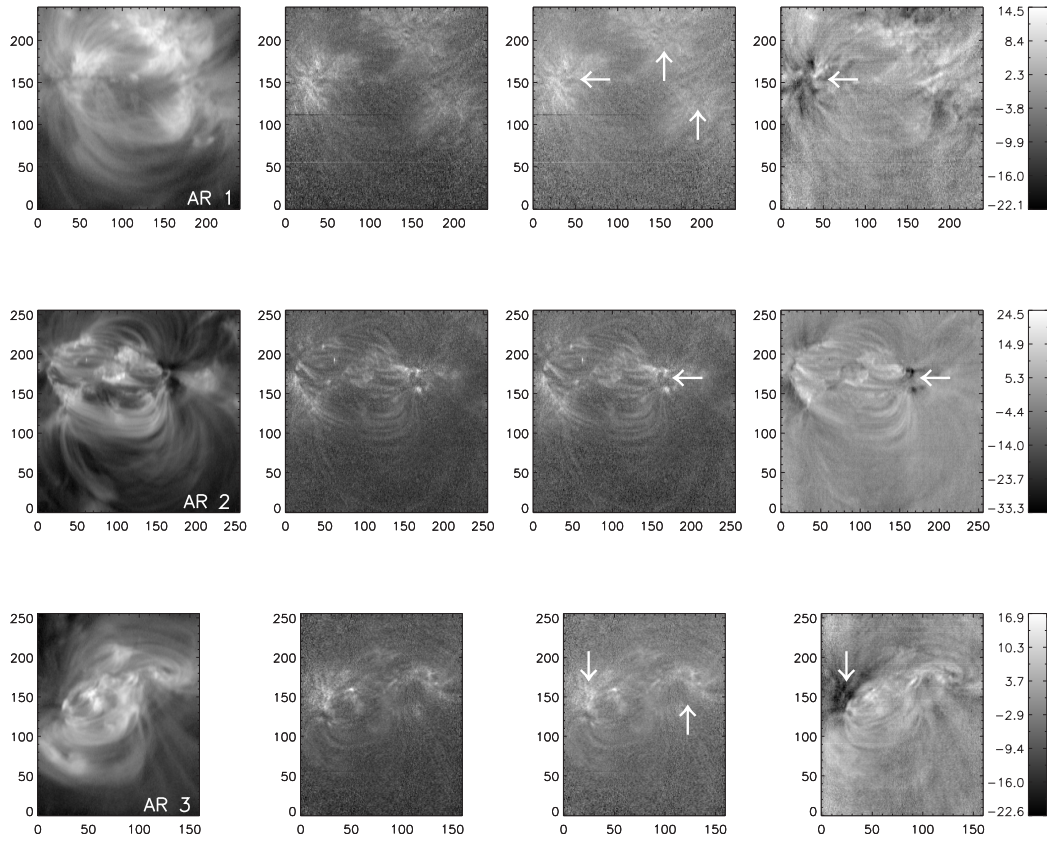


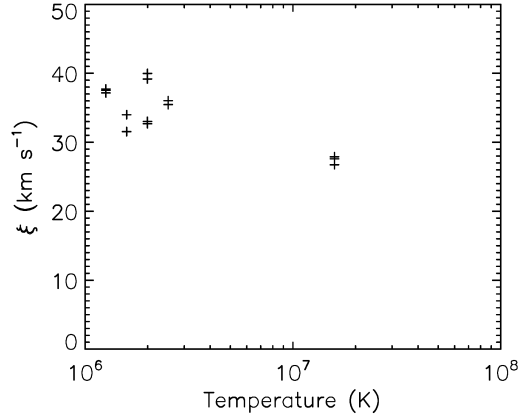
**Fig. 8** Illustrations of the obvious loop structures for the Fe XII  $\lambda 195.12$  line. Top: AR 1. Middle: AR 2. Bottom: AR 3. From left to right, the four columns show the line intensity, line width, nonthermal velocity, and Doppler velocity, respectively. The arrows indicate the footpoints of the loops. The color bars, corresponding to the right panels, are in units of  $\text{km s}^{-1}$ .

zero Doppler velocity is defined as the line centroid averaged over a QS portion. A careful inspection shows that the peaks of the line width (i.e., peak nonthermal velocities) do not fall in the peaks of the line intensity, but are located at the footpoints of the loops. The footpoints also show outflows relative to the surrounding region. After checking more lines, we find that the fact that large nonthermal velocities and outflows occur at the footpoints of loops is basically true for regions with loop structures. If the footpoints are excluded, a stronger correlation between the line intensity and nonthermal velocity can be derived. Table 4 summarizes the coefficients of ARs 1, 2 and 3 for different points representing the spatial elements of loop segments excluding the footpoints. We can see that the coefficients for loop segments are higher than those for the entire region listed in Table 3. Also, the values of each line seem to follow the center-to-limb dependence ( $r_1 < r_2 < r_3$ ), though not so apparent compared with the entire region.

Why is there a stronger correlation between the line intensity and nonthermal motion in loop structures? It could be interpreted in terms of the magnetic field. Owing to the low plasma  $\beta$ , the magnetic field controls virtually all physical processes and observed phenomena in the solar corona. In the loops, the plasma is frozen in the field line and moves with it. Consequently, loops show larger values of correlation coefficients relative to other coronal structures.

**Table 4** Correlation Coefficients between the Line Intensity and Nonthermal Velocity for Loop Segments

Loops	Correlation coefficients		
	Fe XII	Fe XIII	Fe XV
AR 1	0.678	0.291	0.574
AR 2	0.637	0.256	0.713
AR 3	0.630	0.139	0.515

**Fig. 9** Temperature dependence of averaged nonthermal velocities.

### 3.4 Temperature Dependence

Different spectral lines reveal mass motions at different heights in the solar atmosphere. We select seven emission lines to measure nonthermal velocities and compute an average over each of the 12 regions. The seven lines are listed in Table 2. We plot the results of the averaged nonthermal velocity versus temperature in Figure 9. Note that we only keep those points with reliable fitting results. From the figure, we find that the nonthermal velocities seem to display a temperature dependence: they decrease slightly with temperature. Although the lines used in our study are mostly distributed in the higher temperature domain, our result is consistent with the result of Chae et al. (1998). The difference is only that our values of  $\bar{\xi}$  are somewhat larger than theirs. Note that the lines we use have not been included in the work by Chae et al. (1998). The present result also implies that the nonthermal motion becomes weaker with height.

## 4 IMPLICATIONS FOR CORONAL HEATING MECHANISMS

Measurements of coronal lines can shed light on the physical nature of coronal heating. In the following section, we discuss the implications of our results on several possible heating mechanisms.

We have shown that there exists a positive correlation between the line intensity and nonthermal velocity (or line width). Of course, this does not rule out a few cases in which large line widths and nonthermal velocities appear in low line intensity areas. So far, it is not clear why the nonthermal velocity is enhanced with the line intensity increasing. Dere et al. (1984) investigated the correlation between the CIV line intensity and line width and pointed out that the increase in line width at higher intensities can be accounted for in two ways. On one hand, there may exist multiple flows along the line of sight that produce the increased line width. On the other hand, the increased line width may be evidence of

enhanced wave motion that can be dissipated to maintain the transition zone in the regions of highest radiative cooling. To clarify these possibilities, we need to do further research.

Recently, MHD turbulence has attracted increased attention as an interpretation of coronal heating. Chae et al. (1998) summarized three aspects. First, nonthermal motions that are shown to be isotropic in observations are consistent with turbulent motions. Second, the physical conditions in the corona are suitable for the existence of turbulence. Finally, most of the present coronal heating theories require the existence of turbulence because it is very difficult to dissipate mechanical energy without it (see also e.g., Hollweg 1984). Our observations thus confirm this point of view. Nevertheless, the isotropy of nonthermal motions is seemingly in contradiction with pure transverse Alfvén waves propagating along the magnetic field, which are one of the candidates for coronal heating. Since the plasma displacement in such waves is transverse to the field direction, the observed line broadening (nonthermal motions) should vary with the viewing angle. In spite of that, we cannot rule out Alfvén waves as a heating mechanism. The reasons are as follows. First, Alfvén waves are easily excited and they have been identified in the solar wind (Belcher & Davis 1971) by the expected correlation between magnetic and velocity fluctuations. Second, Alfvén waves can provide considerable energy to heat the corona. Most importantly, compressional (longitudinal) waves can be driven by Alfvén waves when the wave amplitude grows (Ofman & Davila 1997, 1998); slow magneto-acoustic waves can be generated by resonant Alfvén waves (Belien et al. 1999). So, the existence of different wave modes makes the observed nonthermal velocity basically isotropic. In addition, the corona is highly inhomogeneous due to the structuring of the magnetic field. It is not paradoxical that MHD turbulence plays a role in heating the corona in combination with Alfvén waves and other physical processes. In other words, for the moment, we cannot distinguish which mechanism provides sufficient energy to the corona judging merely from the nonthermal velocity.

The observed results also suggest that a coherent macroscopic structure between the line intensity and nonthermal velocity may exist (Chae et al. 1998). This implies that small scale flows are at least not the only factor that heats the solar corona. Probably, the heating mechanisms vary from one structure to another. It is unlikely that a pure mechanism heats the corona for a particular region. Our results show a higher correlation between the line intensity and nonthermal velocity in loop structures. There is a need to consider heating mechanisms in different coronal structures. For example, the footpoints may play a crucial role in heating the loop. We find that large nonthermal velocities and outflows exist in the loop footpoints. Therefore, the footpoints are linked to the energy transportation in these regions.

In Section 3.4, we calculate the nonthermal velocities of different emission lines, forming at different heights in the corona. The fact that hotter lines have smaller velocities than cooler lines implies that there is a dissipation of energy. Based on this finding, we can calculate quantitatively the energy flux and compare it with the energy loss rate. This will be done in future work.

## 5 CONCLUSIONS

In this paper, we have measured the line widths and nonthermal velocities in 12 solar regions using high resolution EUV data taken by Hinode/EIS. We obtain the following results. (1) There exists a strong spatial correlation between the line intensity and nonthermal velocity (or line width) for the Fe XII  $\lambda$ 195.12 line and other emission lines. (2) The correlation coefficients show a decreasing tendency from the disk center to the limb. (3) In coronal loop structures, the correlation seems to be stronger. The largest nonthermal velocities occur at the footpoints where outflows appear. (4) The nonthermal velocities of a specific line hardly vary from region to region, which indicates that they are basically isotropic. (5) The nonthermal velocities of hotter lines seem to decrease with increasing temperature.

Based on these results, we have discussed the implications for coronal heating mechanisms. It is reasonable to assume that there is no pure physical process responsible for the heating of the corona in a particular region. Different heating mechanisms may work in different coronal structures. For the coronal loops, the footpoints play a significant role in heating the corona. The fact that nonthermal velocities are isotropic favors the MHD turbulence mechanism. Alfvén waves can also make a contribu-

tion to heating the corona in combination with other wave modes. Dissipation of nonthermal motions is important for coronal heating.

**Acknowledgements** Hinode is a Japanese mission developed and launched by ISAS/JAXA, collaborating with NAOJ as a domestic partner, and NASA (USA) and STFC (UK) as international partners. It is operated by these agencies in co-operation with ESA and NSC (Norway). We are grateful to the Hinode team for all their efforts in the successful launch and operation of the mission. We would like to thank the referee for valuable comments, and thank P. F. Chen, M. Jin, Y. Guo, D. L. Kong and J. Sun for their good suggestions. This work was supported by the National Natural Science Foundation of China under grants 10673004 and 10878002 and by NKBRFSF under grant 2006 CB806302.

## References

- Aschwanden, M. J. 2004, *Physics of the Solar Corona. An Introduction* (Chichester, UK: Praxis Publishing Ltd)
- Belcher, J. W., & Davis, L. 1971, *JGR*, 76, 3534
- Belien, A. J. C., Martens, P. C. H., & Keppens, R. 1999, *ApJ*, 526, 478
- Biermann, L. 1946, *Naturwiss.*, 33, 118
- Boland, B. C., et al. 1975, *MNRAS*, 171, 697
- Chae, J., et al. 1998, *ApJ*, 505, 957
- Cheng, C. C., Doschek, G. A., & Feldman, U. 1979, *ApJ*, 227, 1037
- Culhane, J. L., et al. 2007, *Sol. Phys.*, 243, 19
- Dere, K. P., Bartoe, J.-D. F., & Brueckner, G. E. 1984, *ApJ*, 281, 870
- Dere, K. P., & Mason, H. E. 1993, *Sol. Phys.*, 144, 217
- Doschek, G. A., et al. 1976, *ApJS*, 31, 417
- Doschek, G. A., et al. 2007, *PASJ*, 59, 707
- Doschek, G. A., et al. 2007, *ApJ*, 667, 109
- Gan, W. Q., & Li, Y. P. 2002, *Sol. Phys.*, 205, 117
- Hollweg, J. V. 1984, *ApJ*, 277, 392
- Inverarity, G. W., Priest, E. R., & Heyvaerts, J. 1995, *A&A*, 293, 913
- Kosugi, T., et al. 2007, *Sol. Phys.*, 243, 3
- Mariska, J. T., Feldman, U., & Doschek, G. A. 1978, *ApJ*, 226, 698
- Mariska, J. T. 1992, *The Solar Transition Region* (Cambridge: Cambridge Univ. Press)
- Ofman, L., & Davila, J. M. 1997, *ApJ*, 476, 357
- Ofman, L., & Davila, J. M. 1998, *JGR*, 103, 23677
- Parker, E. N. 1988, *ApJ*, 330, 474
- Schwarzschild, M. 1948, *ApJ*, 107, 1
- Suzuki, T. K. 2002, *ApJ*, 578, 598
- Tsiklauri, D. 2005, *A&A*, 441, 1177
- Zirker, J. B. 1993, *Sol. Phys.*, 148, 43
- Zirker, J. B., & Cleveland, F. M. 1993, *Sol. Phys.*, 144, 341